

Distinct element method analyses of idealized bonded-granulate cut slope

Mingjing Jiang · Akira Murakami

Received: 5 October 2011 / Published online: 1 April 2012
© Springer-Verlag 2012

Abstract This paper presents a numerical study of idealized bonded-granulate cut slope subject to sudden strength reduction. A 2-D Distinct Element Method (DEM) has been used to carry out a simulation of full-process slope failure with focus on very-rapid and extremely-rapid landslide process. The numerical results show that during the landslide process: (1) the soil moves either in a rather random/chaotic way (diffuse failure) or in different curved shear bands (localized failure). The soil close to slope surface moves along downward slope while the soil close to the slope toe moves significantly in the horizontal direction. The landslide experiences very rapid flow most of the time, with its maximum velocity increasing obviously with time at first to its peak value, then decreasing gradually to zero. (2) The soil close to slope undergo a repeated loading and unloading process, and an evident rotation of principal stresses. Their stress state may arrive slightly over the peak strength envelope as a result of extremely rapid flow. (3) There is little grain-size effect for the grains at low velocity, but an evident grain-size effect for the grains at high velocity, with large-size grains tending to move fast. (4) The post-failure inclination is much smaller than the peak/residual internal friction angle of the material.

The post-failure slope surface passes through the centre of the initial slope surface instead of the initial slope toe.

Keywords Cut slope · Distinct element method · Granular soil · Very rapid landslide · Extremely rapid landslide

1 Introduction

Although there are lots of causes leading to instability of earth slopes and the characteristics of the consequent soil movement are usually significantly different, landslide phenomena can be described in three distinct phases: the initiation, the sliding process, and finally the impact of the slide on natural or artificial obstacles [1]. They involve in essence phase changes from solid to fluid at the triggering stage and from fluid to solid when the motion stops. Landslides moving rapidly have a significantly higher possibility of resulting in loss of life and major damage to property than those travelling slowly. As the urban fringe around the world continues to encroach into the surrounding foothills and mountains, the potential loss from the fast landslides will certainly escalate. If they travel into reservoirs, lakes or coastal bays and fords, landslides have the capability of causing large destructive waves [2] or Tsunami.

In addition to theoretical analyses including methods of slices [3,4] and multiple wedges [5,6], slope instability problems are mainly analyzed by two methods:

- (a) Experiments on a granular avalanche in a convex and concave curve chute [7] or on granular flows down a rough inclined plane [8]; physical model tests such as

M. Jiang (✉)
Department of Geotechnical Engineering, College of Civil Engineering, Tongji University, Shanghai 200092, China
e-mail: mingjing.jiang@tongji.edu.cn

M. Jiang
Key Laboratory of Geotechnical and Underground Engineering of Ministry of Education, Tongji University, Shanghai 200092, China

A. Murakami
Graduate Schools of Agriculture, Kyoto University, Kyoto 606-8502, Japan

- centrifuge tests on soil slopes under different conditions, such as rainfalls [9, 10] or shaking [11];
- (b) Numerical analyses mainly by the finite element method [12–14] or by the distinct element method.

Many geotechnical engineering or geo-hazards researchers have employed centrifuge tests to investigate soil slope-slides. Zornberg et al. [15] used centrifuge modeling as a tool for analyzing the behavior of reinforced soil slopes. Nova-Roessig and Sitar [16] studied the dynamic behaviour of soil slopes reinforced with geosynthetics and metal grids, with focus on the failure mechanism and amount of deformations under seismic loading. Katz and Aharonov [17] investigated the type of slope failure and frequency magnitude relations of landslides. They found that different acceleration direction leads to different type of slope failure and heterogeneity may be a major control on the size distribution of natural landslide inventories. Malvick et al. [18, 19] proposed a new method for estimating the susceptibility of a layered, liquefiable, infinite slope to shear deformations associated with void redistribution, in which shear localizations, and water films have been observed in delayed slope failures at interfaces between liquefied sand and lower permeability soil [11, 20]. The loss of shear strength in slopes is potentially affected by void redistribution, whereas a part of the liquefied soil can locally loosen whereas another part densifies [21]. If the loss of strength associated with loosening is able to reduce the undrained strength below that required for stability of the slope, the slope undergoes significant deformations. The deformations may localize along a surface within the dilatant zone where large deformations and discontinuities occur. The mechanics can explain why large deformations delay until after the end of shaking in many case histories [22, 23].

The centrifuge tests as well as the other investigations have enhanced the understanding of slope failure mechanism. Concerned with the initiation, slope failures can be triggered by different causes: (a) changes of effective stresses induced by external load (earthquakes, human action), pore pressures (rainfalls), or changes of geometry (excavation or construction), and (b) material degradation due to weathering and chemical attack [12, 13, 24]. Deformation is sometimes concentrated in a narrow zone, i.e., the failure surface. Kinematics can be approximately described as the movement of a rigid mass along the failure surface. This mechanism of failure is associated with concepts such as material softening, strain localization and progressive failure. Concerned with the sliding process, particularly fast slides, Fell et al. [2, 25], Hunter and Fell [26] and Picarelli et al. [27] stated that there are several classes of soil slope within which a landslide develops into a slide of rapid post-failure: (a) flow slides in saturated (or highly saturated), essentially granular soils that are contractive on shearing under the effective

stress conditions imposed by the slope geometry and pore-pressure conditions; (b) slides in sensitive clays (or quick clays) such as occur, for example, in parts of Scandinavia and Canada; (c) slides in steep cut slopes in residual soil, colluvium or completely weathered rock, either through the soil or weathered rock mass controlled by defects; (d) slides of debris in natural slopes with steep source area slope angles. The pre-requisite of rapid landslide acceleration is always a sudden loss of shear strength. According to the Coulomb strength criterion expressed in Terzaghi effective stresses, this can occur by three processes: (a) loss of cohesion, (b) decreasing of internal friction angle and (c) increasing of pore water pressure. This cohesion may be true cohesion, due to electrostatic forces or chemical cementing, at particle contacts, or apparent cohesion arising from suction forces at particle contacts of unsaturated soils. Failure initiated by cohesion loss will be rapid for steep slopes even if pore-pressure remains unchanged. In comparison, a decreasing of friction will result from particle realignment or asperity breakage in passing from peak to residual friction angle. This process is not very effective to lead to acceleration of slide since the decline of friction usually requires long displacement. In cases where liquefaction occurs, the mobilized stress angle is smaller than that of Coulomb's. When a loose and saturated sand specimen is loaded under an undrained condition, it may become unstable leading to a static liquefaction behavior. Static liquefaction or instability of loose sand under undrained conditions is one of the most frequent causes of flow failures in granular soil slopes. This type of instability behavior is microscopically characterized by a sudden collapse of a soil structure accompanied by a rapid increasing of pore pressure well. Recent results also show that the debris flows mobilized from initially dense soils during which the arresting effect of negative pore pressures generated by dilation is greatly reduced as the dilatant soils approach their critical void ratios [28].

Numerical analysis using the finite element method (FEM) is a powerful tool in predicting slope failure in geotechnics and is able to model non-linear problems [29], in which a failure criterion [30, 31] or a material instability [1] was used based on elasto-plasticity. It can also be used to model diffuse failure mechanisms of catastrophe landslides of an embankment on a collapsible soil (one of bonded materials) under earthquake loading [24]. However, from a mathematical point of view, the inception of a shear band is characterized by a discontinuity in the strain field, which can evolve towards a discontinuity in the displacements at a later stage. Much effort has been devoted during the past years to better understand this phenomenon, but the problem is ill-posed for elasto-plastic materials and the results obtained in numerical models depend on the mesh size and alignment. In addition, concerned with mathematical modeling of landslides, there is still much work to be done to describe coupling between

different phases, and phenomena such as segregation and combination.

A tool that appears to be promising for investigations on landslide process of granular material, particularly that of very rapid or extremely rapid landslide, is the distinct element method (DEM), which is a numerical simulation technique originally developed by Cundall and Strack [32]. Unlike FEM, this technique treats soils as an assembly of discrete elements, starts with basic constitutive laws at inter-particle contacts and can provide macroscopic and microscopic responses of the particle assembly under different loading conditions. DEM has been employed to examine several aspects of soil behavior, such as granular mechanics [33–35], creep theory [36] and anisotropy [37] of soils, mechanics of crushable soils [38,39], constitutive models for granular material [40,41], the effective stress and shear strength functions of unsaturated granulates [42], yielding of micro-structured soils under 1-D compression and biaxial tests [43–47]. It has also been employed to investigate boundary value condition problems such as penetration mechanism of cone-penetration tests [48,49]. It is used to simulate the flow regimes to investigate the interaction between rapid granular flow and an obstacle [50], snow avalanches [51,52], and slope instability [53–55]. Few works have been found on landslide mechanism, particularly during the whole very rapid or extremely rapid landslide process from microscopic and macroscopic point of view, of idealized bonded-granulate cut slope by DEM analyses. This constitutes one of strong motivations in this study.

The main objective of this paper is to numerically study idealized bonded-granulate cut slope subject to sudden reduction of bond strength by DEM analyses. For this purpose, a two-dimensional (2-D) DEM code, namely NS2D developed by one of the authors [43,44,46,48], is used. Deformation, velocity and stress fields as well as displacement and stress paths are analyzed via painted grids, velocity/stress vector distributions etc. during the whole landslide process. The main limitation of the DEM is its inability to simulate an actual model of millions of particles with the current PC. Note that landslide mechanism of idealized slope obtained here would be helpful for understanding natural landslide and there is no intention here to directly relate the all numerical results to field prototype quantitatively. Although many other simulations were carried out, only one full and typical simulation of landslide is presented in this paper which is enough to clarify the very rapid landslide mechanism. Grain crushing, which will lead to the low average apparent-friction angle in rapid landslides [56], is not taken into account. In addition, a full comparison with experiments, FEM code or a theoretical model is not included, because there is few data on very rapid or extremely rapid landslide.

2 Landslide test simulated by DEM

2.1 The DEM code

The 2-D DEM code used herein is NS2D, which is in essence similar to that proposed by Cundall and Strack [32] and which is developed for natural soils, unsaturated soils and rough sands [42–44,46]. In the code, each rigid disk is identified separately, with its own mass, moment of inertia and contact properties for different kinds of soils. For bonded granulates in this study, we chose the simple bond contact model shown in Fig. 1, which consists of a normal (tangential) component to resist traction (shear) force, but neglects bond rolling resistance [46]. As shown in Fig. 1, the normal and tangential components of the model are similar in their principle. They both include a spring reflecting an elastic behavior of the bond before failure and a dashpot that allows energy dissipation and quasi-static deformations in DEM analyses. Unlike the standard contact model [32], both the normal and tangential contact models include a rigid bond element which is set to represent the main action of bonding materials. The normal model includes a divider to simulate the fact that no traction force is transmitted through the contact when the bond is broken and the particles are separated. The tangential model includes a slider that provides the contact a shear resistance controlled by the Mohr–Coulomb criterion. Note that the physical model for bonds in Fig. 1 will reduce to the standard contact model [32], when the bond elements are broken or of zero bond strength.

2.2 Bonded granular ground

The material used in the bonded granular cut slope ground is composed of twenty types of disks with maximum and minimum diameter being 3.525 and 2.25 mm respectively, as shown in Fig. 2. It has an average grain diameter

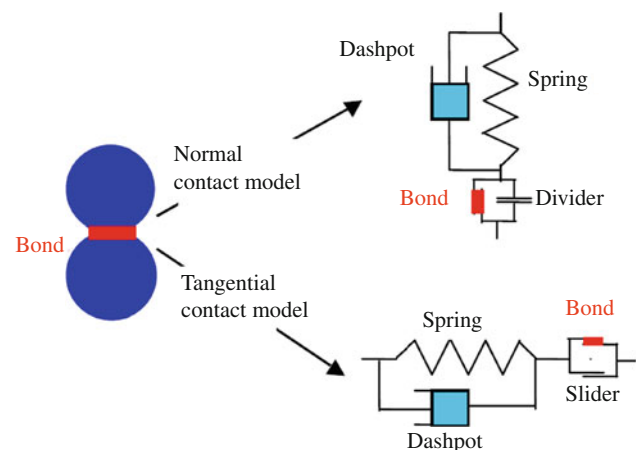


Fig. 1 Contact models of bonded granulates used in the DEM analyses

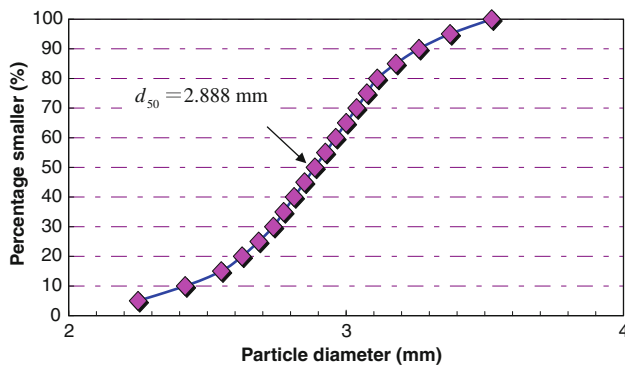


Fig. 2 Distribution of grain size used in the DEM landslide analyses

$d_{50} = 2.888$ mm and uniformity coefficient $d_{60}/d_{10} = 1.23$. The cut slope is generated by excavating a target ground, which consists of 20,000 particles with planar void ratio of about 0.26, and has a depth and width as $94d_{50}$ and $201d_{50}$ respectively. The multi-layer under-compaction method proposed by one of the authors [57] was employed to generate the ground at first:

The ground is generated by compacting four layers of particles. For each layer, 5,000 particles are randomly distributed in an area corresponding to a width of $201d_{50}$ and a planar void ratio of about 0.65, and then statically compacted. In the compaction, the side and bottom rigid walls are fixed and the top wall moves downward at a constant speed till the void ratio is equal to 0.26. The wall-particle is frictionless in order to improve the homogeneity, while inter-particle frictional coefficient ($\tan \phi_{\mu}$) is chosen to be 1.0 in order to produce a medium assemblage of particles.

In order to produce the identical void ratio in all the layers to the final average planar void ratio \bar{e}_{pf} , compact the bottom layer, 1, at a void ratio $e_{p(1)}$ larger than \bar{e}_{pf} ; the second layer, 2, in such a way that the layers 1 and 2 have an average void ratio $e_{p(1+2)}$ larger than \bar{e}_{pf} , etc...until the final layer, which is directly compacted at $e_{p(1+2+\dots+n)} = \bar{e}_{pf}$. The distribution of $e_{p(1)}, e_{p(1+2)}, \dots, e_{p(1+2+\dots+n)} = \bar{e}_{pf}$ was selected by following an equation suggested in [57], i.e., $e_{p(1)} = 0.28, e_{p(1+2)} = 0.27, e_{p(1+2+3)} = 0.265, e_{p(1+2+3+4)} = 0.26$.

After the sample was generated, reduce $\tan \phi_{\mu}$ to a value of 0.5, a typical value used in DEM analyses. Then the sample was allowed to settle in an amplified gravity field of 1,000 g in a way similar to centrifuge modeling to simulate a moderate slope later. Finally, the top wall was removed away to simulate a free top boundary of the ground, while the remaining side and bottom walls were all kept as frictionless.

After the unbonded ground was prepared at the required density, all particle contacts were bonded with a set of bond model parameters for further testing. For simplicity, we shall investigate the landslide mechanism of the cut slope in which the bond strength reduces abruptly to zero at all contacts

between particles. Hence, it has been considered in the present study that $Rnb = Rtb = R$, with a value of 30 MN/m. The normal and tangential spring stiffnesses are taken to be 1.5×10^9 and 1.0×10^9 N/m respectively. It is expected that the slope failure initiated by such a loss will be rapid. Figure 3a presents the DEM bonded granular ground, which was painted into rectangular grids with different colors for the analyses of deformation.

Note that with 2 viscous local damping in the normal and tangential directions, there should be some viscous effects in the numerical macroscopic responses, and the numerical time will not coincide with the physical time if inappropriate damping value is used. In our study, the damping value was determined by simulating a repose angle test on the same unbonded granular material under the same amplified gravity as those used in the paper. In the simulation, an assembly of unbounded grains drops freely down under 1,000 g to ground, which is simulated by a rigid wall that has the same contact behavior as inter-particle contacts. Different damping values were used in trial simulations, from the small to the large, and the simulated results were compared with experimental observation. It was found that if the damping value was very small, lots of grains would rebound into space over the ground after they contacted with it, and the repose angle test could not be simulated well. With the damping value gradually increased in the test, fewer and fewer grains would rebound into space. Once no grains rebound into space and the repose angle test can be simulated well, the damping value will be used later in the slope-slide analyses in which the numerical time will coincide mostly with the physical time.

2.3 Boundaries in bonded-granular cut slope

After the bonded granular ground is generated, a block of particles, defined by ABCD in Fig. 3a, is excavated from the ground. After the excavation, a cut slope is formed with the slope height and slope inclination being $42d_{50}$ and 45° respectively as shown in Fig. 3b. The choice of the slope inclination is based on the understanding that if the slope is sufficiently steep, the post-failure velocity is likely to be rapid regardless of the soil properties [2] and change of pore water pressure. In addition, the distance between slope toe B and side boundary wall, i.e., AB in Fig. 3b, is $75d_{50}$, and the slope bottom is $52d_{50}$ distant to the bottom boundary wall. The DEM simulation in this study is in essence similar to granular slopes in centrifuge modeling. Hence, several factors have been taken into account in choosing slope and ground sizes here in a similar way to centrifuge modeling, such as boundary effects, scale effects, grain size effects (e.g., [58,59]). In addition, current PC capacity has also been considered to make the simulations practical.

time is much smaller than the time of propagation, the material behaves as ‘drained’.

- (b) Flow of slurries with a high water content, where the time of dissipation is much higher than that of propagation. The behaviour can be assumed to be of undrained type. Material behaviour can be approximated using rheological models [12, 13].

2.4 Observation methods

In addition to four biaxial compression tests on the unbonded ground material to measure its mechanical properties, one full landslide analysis has been carried out on the cut slope with its strength reduced abruptly to zero at all inter-particle contacts. In the slope slide simulation, landslide mechanism is continually investigated by deformation patterns, displacement paths, maximum velocities, total kinetic energy, velocity vector distributions, stress fields and stress paths defined as below.

2.4.1 Coordinates

Several aspects are to be investigated at different time in the process of landslide in this study. The common point O between the left-hand side wall and the bottom boundary wall is selected as the origin. The positive X-axis is chosen to be along the bottom boundary wall towards the right-hand side wall in Fig. 3, while the positive Y-axis is chosen to be along the left-hand wall towards the ground surface. For convenience in the analysis, the position is further normalized by the average grain diameter d_{50} and expressed in the unit (d_{50}) in the following sections.

2.4.2 Painted grids

In order to describe landslide process clearly, we painted the initial ground into grids with seven different colors before the excavation starts. The painted grids are observed and output to reflect the deformation pattern of the cut slope in analogous to the finite element analysis (FEA), at different time. Each grid of particles is painted with a specific color and this color is then maintained unchanged. As shown in Fig. 3a, the ground is painted into 544 quadrilateral grids of four ‘nodes’ before excavation, which are similar to quadrilateral elements commonly used in FEA. Each grid has an initial width and height close to $6d_{50}$, and is composed of about 37 particles. The grid size is chosen by considering that:

- (a) It should be small enough to capture the high gradients of variables in the landslide;
- (b) It should be large enough to represent a ‘continuum element’ from the viewpoint of micro- and macro-mechanics [40].

2.4.3 Displacement paths

In this study, displacement paths are traced at the particles which are located at ‘grid nodes’ and distributed horizontally on lines 1–4 in Fig. 3b. These lines are located at different depths. Line 1 is one grid below the slope top, line 2 through the middle of the slope, line 3 through the slope toe and line 4 one grid below the slope bottom. The particles at these nodes are traced continuously in order to reflect the variation of displacement path in the cut slope during landslide, see Fig. 9 below.

2.4.4 Velocity-vector distributions

In order to understand the landslide mechanism well, we shall output visually velocity vectors of all particles in different colors as velocity distributions, see Fig. 12 below. The quasi-static velocity of each particle is computed by its position change of particle centre between the current time and previous time. Based on the maximum velocity v_{\max} measured, each velocity vector is painted with different colour which is based on its value and defined in Fig. 4. v_{\max} is divided by seven in this study. Hence any velocity will lie into one of the seven groups, and is painted with a corresponding color shown in Fig. 4.

2.4.5 Stress fields

In addition to the variables concerned with the motion of particles, the landslide mechanism is also investigated via stress fields and stress paths. The average stress tensor σ_{ij} is calculated over a volume V [32].

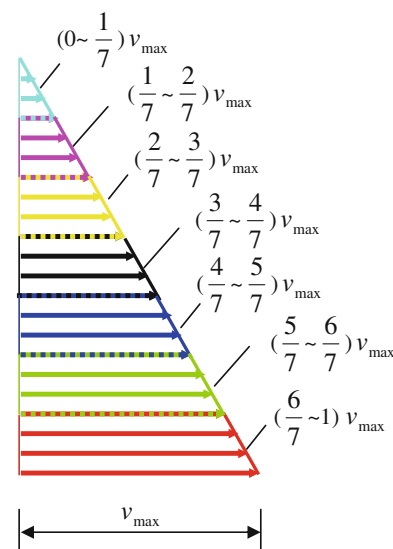


Fig. 4 Representation of colors for velocity vectors in the DEM landslide analyses

$$\sigma_{ij} = \frac{1}{V} \sum_{k=1}^N r_k \sum_{c=1}^p l_c^i F_c^j \quad (1)$$

where F_c^i and l_c^j are the contact force vector and contact orientation vector respectively at contact c of particle k . r_k is the radius of particle k . N is the number of particles in V and p is the number of contacts on particle k .

The stress tensor is calculated by Eq. (1) over a constant volume V about $1,000 \text{ mm}^2$ centered at grid nodes shown in Fig. 3b, which includes about 100 particles. In the light of extremely large deformation of the soil in landslide, two aspects have been considered in choosing the centre of V in order to obtain accurate stress fields and stress paths: (a) it is located at a grid node, and moves with the node; and (b) the grid nodes on the initial ground boundaries or the slope surface are excluded. The first aspect indicates that the average stress tensor is calculated on current configuration and hence corresponds to the Cauchy stress tensor used in continuum mechanics. The second aspect is to avoid such a fact that only about half of V is filled with particles and hence Eq. (1) will give rise to inaccurate value if its centre locates at the boundaries. In order to reflect the main features of the stress fields and stress paths, the stress tensor calculated is further used to obtain the major (minor) principal stress, σ_1 (σ_3), where compression stress is taken as positive, as well as the inclination θ of major principal stress to Y -axis, by

$$\begin{aligned} \frac{\sigma_1}{\sigma_3} &= \frac{\sigma_{11} + \sigma_{22}}{2} \pm \sqrt{\left(\frac{\sigma_{11} - \sigma_{22}}{2}\right)^2 + \sigma_{12}^2}; \\ \theta &= \frac{1}{2} \arctan\left(\frac{2\sigma_{12}}{\sigma_{11} - \sigma_{22}}\right) \end{aligned} \quad (2a,b)$$

We shall output visually the distributions of major (minor) principal stress vectors in the slope at different time, see Fig. 13 below. In addition, the stress paths at positions 1–5 shown in Fig. 3b are traced continuously during landslide, which are initially located along slope surface or slope bottom. We shall describe the stress paths at these positions by (a) mean stress $\sigma_m = (\sigma_1 + \sigma_2)/2$; (b) deviatoric stress $\sigma_s = (\sigma_1 - \sigma_2)/2$; and (c) the change of θ , see Figs. 14 and 15 below.

3 Basic features of tested material

3.1 Mechanical behavior of unbonded material

Since this paper is to study landslide mechanism of idealized bonded-granular slope after sudden reduction of bond strength, it is important to measure the mechanical behavior of unbonded material at first. Figure 5 presents the relationships of deviatoric stress versus axial strain, and volumetric strain versus axial strain of the ground material which

bond strength has reduced to zero. These relationships were obtained from four biaxial tests with compression strain rate = 1.0%/min on a 5,000 particle specimen. The consolidation stress is 50, 100, 200, 400 kPa respectively, by following China Code on Geotechnical Tests, which covers the initial stress state of the ground (to be introduced in the next subsection). Figure 5 shows that the material has a strain-softening behaviour accompanied by dilatancy in this conventional stress path, a typical feature demonstrated by medium-dense sands. The peak (residual) strength envelope of the material deduced from these biaxial compression tests are provided in Fig. 6, indicating that the material is of a peak (residual) internal friction angle 22.2° (18.8°). The friction angles are thus small in comparison with the coefficient of interparticle friction of 0.5 ($\phi_\mu = 26.5^\circ$). Such a small value is normal since the models ignore the possibility of particle rolling resistance at contacts [46].

3.2 Initial stress field in the ground before excavation

To understand idealized bonded-granular cut slope, Fig. 7 provides the variations of horizontal and vertical stresses in the ground before the excavation starts. The horizontal and vertical stresses in Fig. 7 are the average of all values measured at each depth. Figure 7 shows that the initial vertical stress increases linearly with depth from 0 Pa to about 500 Pa. The initial horizontal stress increases linearly with the distance to the ground surface at first with the ratio of horizontal stress σ_x to vertical stress σ_y being about 0.62, then deviates from this linearity slightly. This non-linearity near the bottom wall is slightly beyond the expectation of the K_0 condition in a semi-infinite half-space ($K_0 = \sigma_x/\sigma_y = 1 - \sin \varphi = 0.62$), but has been reported in physical experiments on retaining walls for a finite media. Note that the initial stress state falls into the consolidation stress range introduced in the previous subsection as designed.

4 Observations in DEM landslide simulation

Landslide phenomena can be described in three distinct phases: the initiation, the sliding process, and finally the impact of the slide on natural or artificial obstacles [1]. Fast landslides and debris flows are geophysical, gravity driven flows causing extensive loss of human live and economic damage in the world every year. Debris avalanches start as localized failures of perhaps a few cubic meters of soil, grow in width as they propagate down slope, increasing in volume many times beyond the magnitude of the initial slide. One of the best documented examples of such a slope failure is the largest known natural rapid landslide in Hong Kong, the Tsing Shan debris flow of 1990 [61]. However, the information is not enough to clarify the full landslide process

Fig. 5 Relationships of deviatoric stress versus axial strain (a), and volumetric strain versus axial strain of the material without bond strength, measured in DEM biaxial tests under different consolidation stress and a constant compression strain rate = 1.0 %/min

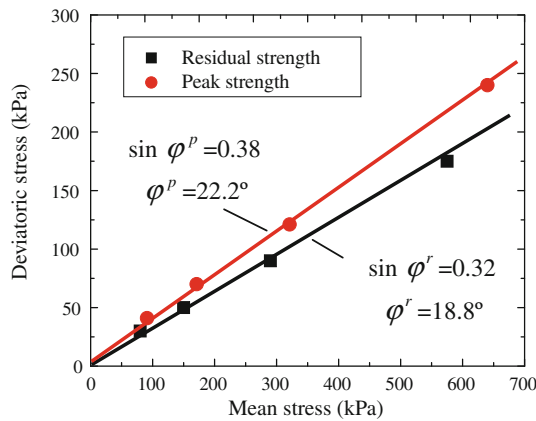
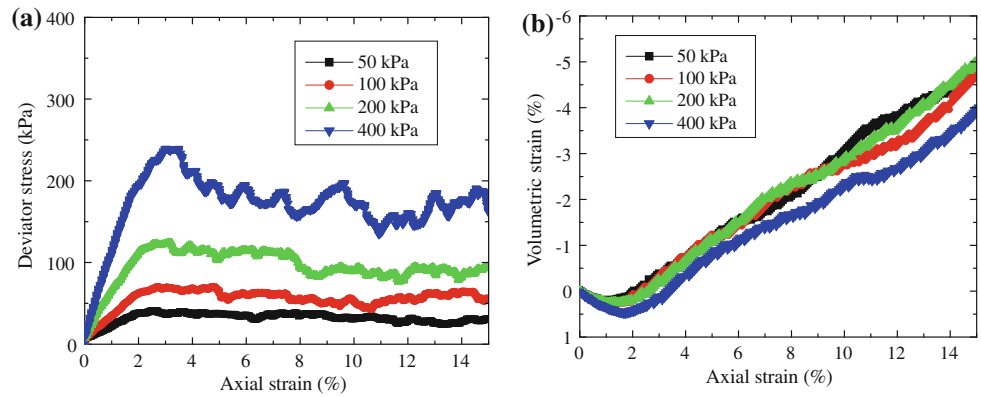


Fig. 6 Peak and residual strength envelopes of the material without bond strength deduced from the DEM biaxial tests

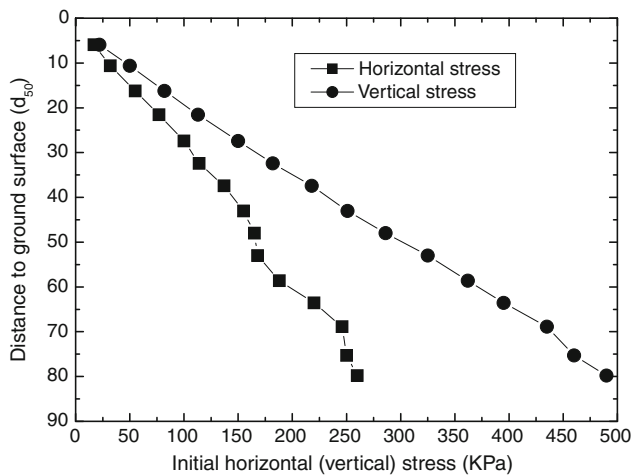


Fig. 7 Initial vertical and horizontal stresses measured in the DEM bonded granular ground

as a result of technological difficulty. In this section, we shall investigate the full very-rapid landslide process from the viewpoints of the deformation pattern, displacement paths, velocity fields, stress fields and stress paths.

4.1 Deformation patterns

4.1.1 Painted grids

Figure 8 presents the painted grids of the DEM cut slope at different time after its bond strength reduced to zero. Figure 8 shows that 6 s after excavation, deformation of the grids about slope, particularly those about slope toe and slope top, is large enough to be told by the naked-eyes. These deformed grids can be properly described by the ‘elements’ in the conventional finite element analysis (FEA). Fourteen seconds after excavation, deformation of the grids about slope is so large, with the grids about slope toe peculiarly extended and twisted (which means the soil here moves forward from the initial position), that the shapes of grids appear to be very difficult to be described properly with the ‘elements’ used in conventional FEA. Then, deformation of soil about slope is so large that it cannot be described with the grids in continuum mechanics. Instead, an unstable slope is formed and changes continuously, with the soil about the new slope consisting of different colors of particles in mixture. A new stable and gentle slope is formed 50 s after excavation with the distance between the new slope toe and the side boundary wall being $23d_{50}$, which is far less than the initial value $75d_{50}$.

4.1.2 Displacement paths

Figure 9 plots the displacement paths of grid nodes on lines 1–4 in the DEM landslide analyses, which are located one grid below slope top, through the middle of the slope, through slope toe (i.e., slope bottom) and one grid below slope toe respectively. Figure 9a shows that final positions of the nodes on line 1 are all below their initial positions. The nodes of $X/d_{50} > 160$ move downward slightly. In contrast, those grid nodes of $X/d_{50} < 160$ moves downward and sideward (along downward slope), in a manner that the closer to the slope surface, the larger the displacement. Similar phenomenon is also found on line 2. In contrast to Fig. 9a, b shows

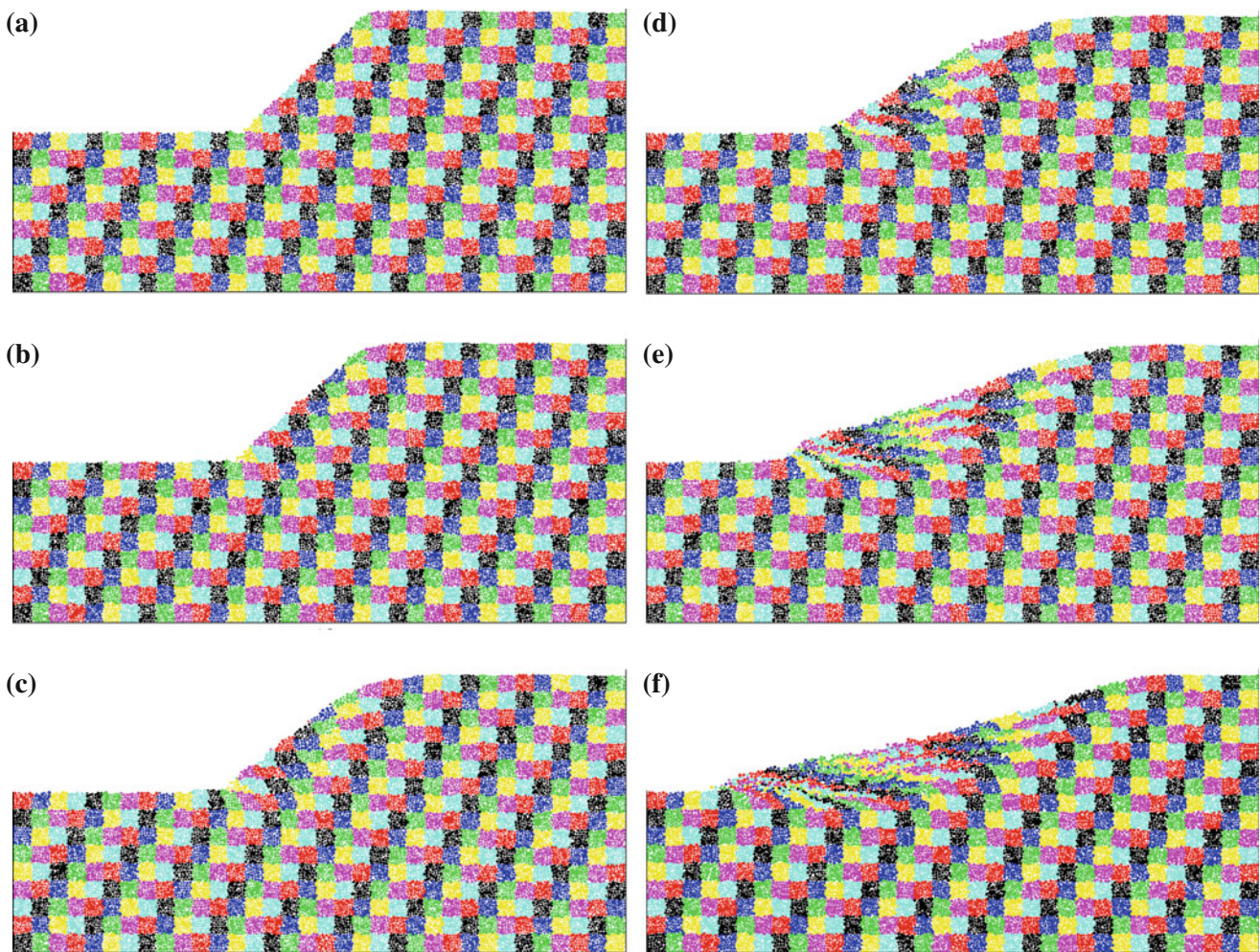


Fig. 8 Painted grids of the DEM cut slope measured at different time after its bond strength reduced to zero. **a** $t = 6$ s, **b** $t = 10$ s, **c** $t = 14$ s, **d** $t = 20$ s, **e** $t = 30$ s, **f** $t = 50$ s

that the grid nodes on line 3 move in different manners at different positions. The grid nodes of $X/d_{50} > 100$ on line 3 (i.e., those inside the initial slope but far from the slope toe) undergo slight upward and sideward motions. The nodes of $75 < X/d_{50} < 100$ on line 3 (i.e., those inside the initial slope but close to the slope toe) move significantly in horizontal direction. However, the nodes of $20 < X/d_{50} < 75$ on line 3 (i.e., those outside the initial slope but inside the new slope) move upward at first and then downward while experiencing significant horizontal motion. In addition, Fig. 9b shows that the grid nodes on line 4 undergo slight motions. This is in agreement with the previous study using the dynamic flow model DAN [62] that significant initial acceleration will propel the toe of the landslide mass forward, overriding the ground surface down slope. Note that DANs appear inaccurate when the flow is 3D, particularly when hitting an obstacle, and it is beyond the capacity of current PCs to simulate 3D flow with DEMs. Hence, there is no intention in this paper to analyze 3D flow.

4.2 Velocity fields

It is important to consider the post-failure velocity because there is a much greater chance of loss of life for rapid than for slow-moving slides. Figure 10 provides the variations of the maximum velocity of grain against time measured in the DEM landslide analyses. Figure 10 shows that the velocity increases obviously with time at first to its peak value 0.055 H/s at time $t = 28$ s, where H is the slope height of the model. Then it decreases gradually with time. Almost none of grains move when $t = 90$ s. This is in agreement with the mechanical insight of landslide phenomena [1] that landslides involve in essence phase changes from solid to fluid at the triggering stage and from fluid to solid when the motion stops. Moreover, according to the suggestion given by the International Union of Geological Sciences [63], the terms ‘very rapid’ and ‘extremely rapid’ are used for the velocity ranging from 3 m/min to 5 m/s and the velocity higher than 5 m/s respectively, which

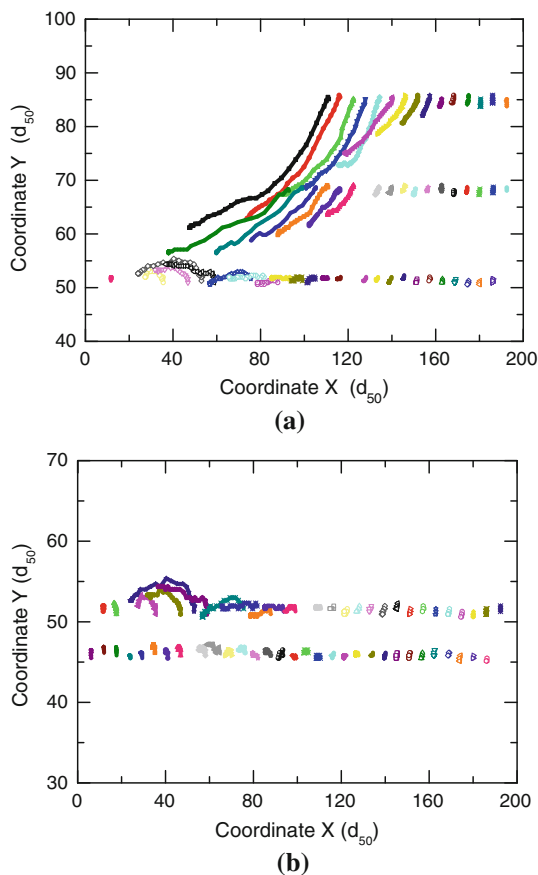


Fig. 9 Displacement paths of grid nodes on lines 1–4 in the DEM landslide analyses. **a** Displacement path of particles initially on lines 1–3. **b** Displacement path of particles initially on lines 3–4

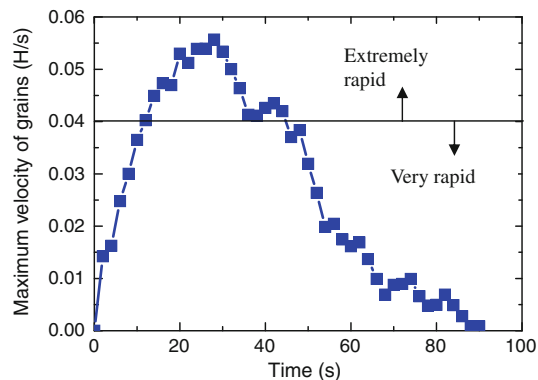


Fig. 10 Maximum velocities of grains measured in the DEM landslide analyses

corresponds to that from 0.00041 H/s to 0.041 H/s and that over 0.041 H/s in this paper, where H is scaled up by 1,000 since 1,000g was used in the simulation. Hence, Fig. 10 shows that the landslide experiences very rapid flow two third of the time, and extremely rapid flow one third of the time.

Figure 11 presents the distributions of velocity vectors measured at different time after excavation in the DEM landslide analyses. Figure 11 shows that the distribution differs evidently at different time, which is mostly characterized with shear bands and translation-rotation of the body above the shear bands. At $t = 4$ s, i.e., 4 s after excavation, the material slides either in a rather random/chaotic way (diffuse failure) [53] or in different curved shear bands (localized failure). The closer to the slope surface, the faster the material moves in diffuse failure, while the farther to the slope, the more curved is the band which appears to share the same symmetric line. In addition, the slope top moves downward slightly. The material continues to slide in the similar manner till $t = 10$ s, while the slope top stops moving downward. From $t = 10$ s to $t = 40$ s, the material still slides in either in diffuse failure [53] or in different curved bands which symmetric lines are not the same, and the particles in the low position move fast. At $t = 50$ s, the material that slides in fewer and different curved bands shares the same symmetric line. Finally, at $t = 60$ s, only a few of particles on the new slope surface move down slope in a rather random/chaotic way. Note that the observation in Fig. 11 is obviously different from that obtained from finite element analysis in which a slope was subjected either to a traction or to a small perturbation [1]. However, a chaotic field has already found by Darve et al. as a kind of failure in granular material [53]. Moreover, the observation on the curved shear bands in Fig. 11 is in a good agreement with the experimental investigation on granular surface flows in a narrow channel, in which a uniform flow is localized in the free surface with the exponential evolution of the velocity profile in the flowing layer [64]. This exponential evolution is the main feature of the gravity-induced shear flow with free surface which can be interpreted by a continuum model [65].

In the next sub-section, we shall investigate the very-rapid landslide process from the viewpoint of stress fields and stress paths.

4.3 Stress fields and stress paths

Figure 12 provides the distributions of principal stress vectors measured at different time in the DEM landslide analyses. Note that in the figure, the maximum major stresses are plotted by a vector of a constant length in order to illustrate the distributions clearly. Figure 12 shows that although distribution of principal stress vectors is different at different time, depending on the shape of slope, there are several common features: (a) the major principal stress is in the horizontal direction in the area close to the left boundary wall, but in the vertical direction in the domain close to the right boundary wall. Its inclination lies between 0° and 90° in other area, about 45° in the area close to the slope surface. (b) The maximum stresses occur in the area close to the

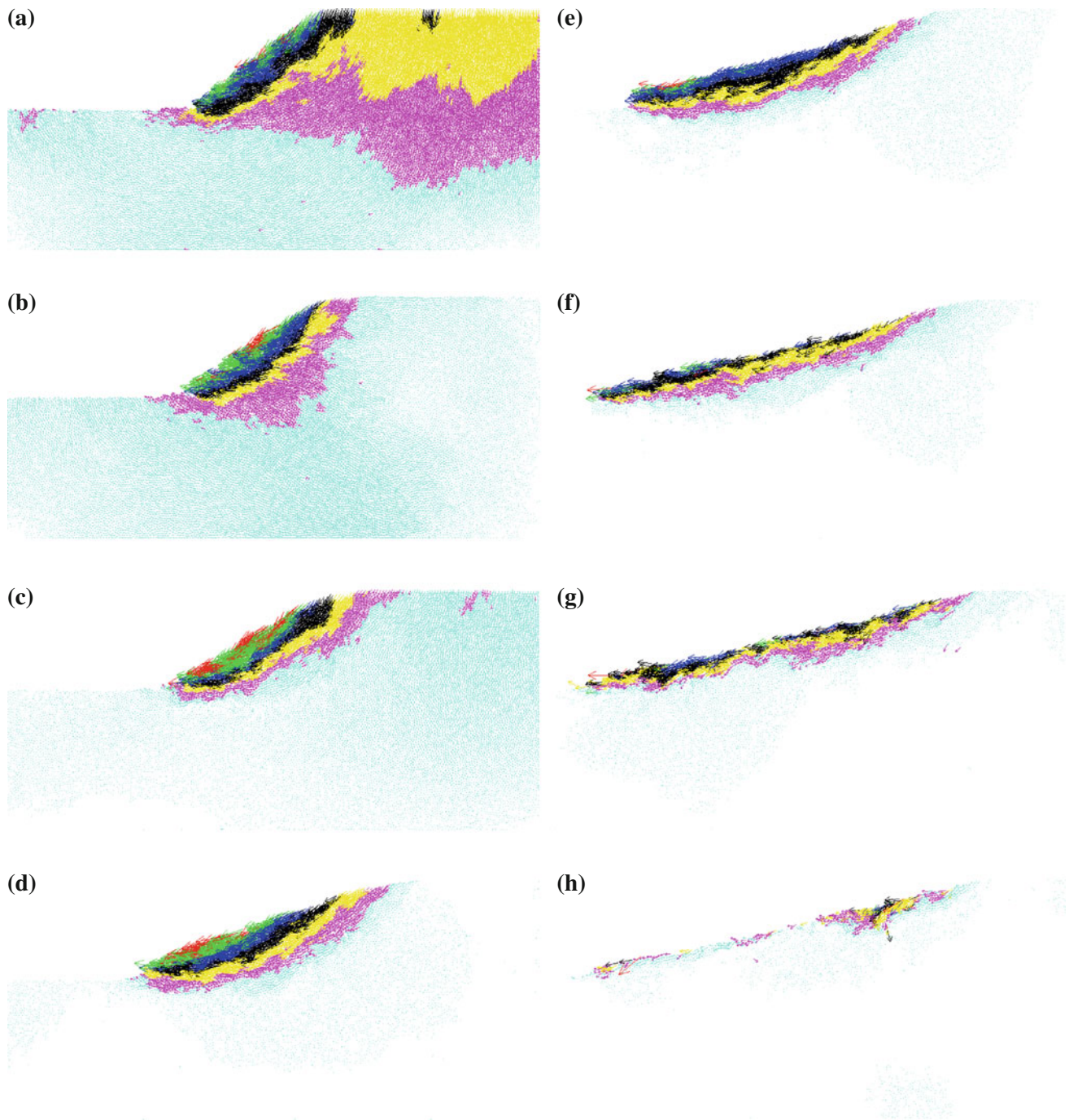


Fig. 11 Distributions of velocity vectors in the DEM landslide analyses **a** $t = 4$ s, **b** $t = 6$ s, **c** $t = 10$ s, **d** $t = 20$ s, **e** $t = 30$ s, **f** $t = 40$ s, **g** $t = 50$ s, **h** $t = 60$ s

bottom boundary wall, and the minimum stresses occur in the area close to the free surface.

It is believed that the knowledge of the stress path is necessary to accurately predict the potential for flow failure of soils [66]. Figure 13 provides stress paths observed at Positions 1–5 shown in Fig. 3b in the DEM landslide analyses, which are expressed in the mean stress-deviatoric stress space. In

addition, the peak strength envelope of the material obtained from the biaxial compression tests is presented in the figure. Figure 13 shows that during the landslide process all the five points undergo a repeated loading and unloading process, i.e., fluctuations. The fluctuations are due to local avalanches, whose local movements are neither continuous nor regular, but sudden and with velocity discontinuities.

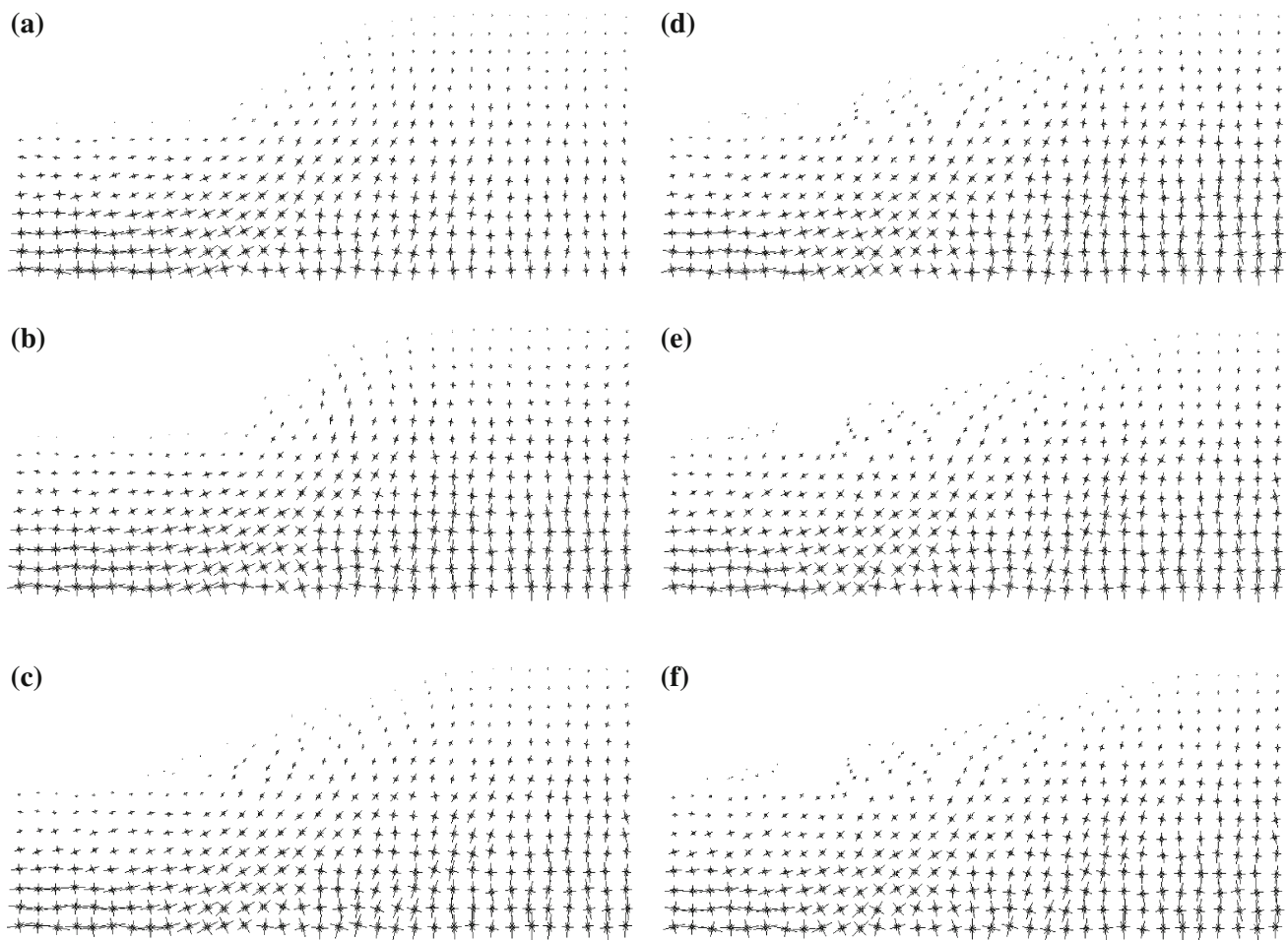


Fig. 12 Distributions of principal stress vectors in the DEM landslide analyses **a** $t = 4$ s, **b** $t = 6$ s, **c** $t = 10$ s, **d** $t = 20$ s, **e** $t = 30$ s, **f** $t = 40$ s

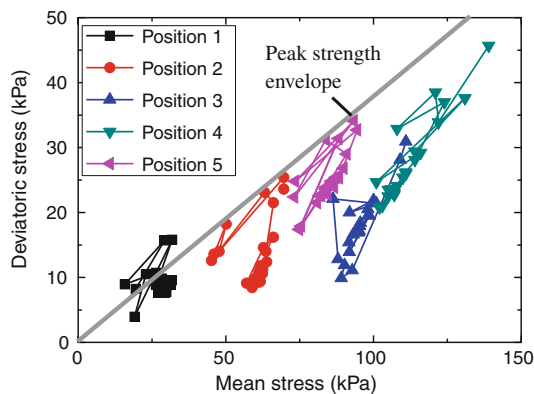


Fig. 13 Stress paths observed at Positions 1–5 in the DEM landslide analyses

Such fluctuations may lead to dynamic pore-pressure fluctuations in rapidly shearing water-saturated granular materials in practice, which has already been observed in the rapidly shearing tests and in the artificial landslides [67]. Moreover, it is interesting to note that the stress state of the

soils located at Positions 1, 2, 5 arrive slightly over or at the peak strength envelope. This appears to be reasonable, since granular materials also show some rate-dependent behavior (e.g., [41]) which indeed has been reflected by a viscous term in the contact laws in the DEMs. The strength envelopes are obtained from the biaxial compression tests with compression strain rate at 1%/min. It is probable that soil located at Position 1 undergoes large deformation accompanied by the strain rate larger than 1%/min during extremely rapid landslide. Moreover, there are inertial effects during landslide process, which will lead to the stress states over the peak strength envelope as well. In contrast, the stress state of the soils located at Positions 3–4 is still below the peak strength envelope.

Figure 14 presents the rotation of principal stresses observed at the same 5 positions as shown in Fig. 13. Figure 14 shows that the soils at all positions undergo an evident rotation of principal stresses, all of which finally approaches a value about -40° , where counterclockwise rotation is taken as positive. Such rotations may be another reason leading to dynamic pore-pressure fluctuations in rapidly shearing

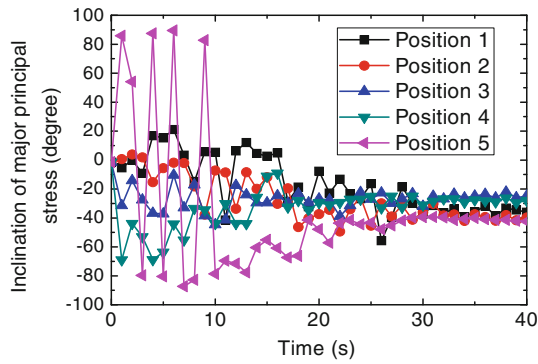


Fig. 14 Rotation of principal stresses observed at Positions 1–5 in the DEM landslide analyses

water-saturated granular materials observed by Iverson and LaHusen [67] as a result of their noncoaxiality. Moreover, before principal stresses rotate to this final value at $t = 30$ s, the soil at different positions rotates in a different cyclic way.

5 Discussion

In this section, we shall discuss the very-rapid landslide process from the viewpoints of the kinetic energy, velocity range, grain-size effect and post-failure configuration.

5.1 Kinetic energy

Total kinetic energy of grains can be possibly used to evaluate the safety of natural or artificial obstacles. Figure 15 provides the total kinetic energy of grains measured at different time in the DEM landslide analyses, which is computed by taking into account the translational kinetic energy and the rotational one of all grains and which has also been used recently by Nicot et al. in [68] as follows.

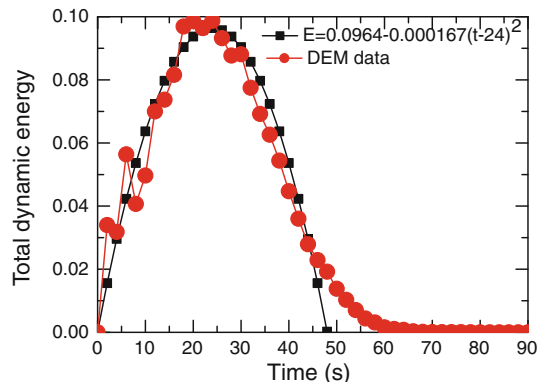


Fig. 15 Total kinetic energy of grains measured in the DEM landslide analyses

$$E = \sum_{i=1}^M \frac{1}{2} (m_i v_i^2 + I_i \omega_i^2) \tag{3}$$

where m_i , I , v_i and ω_i are mass, inertia, translational and rotational (angular) velocities of grain i respectively. M is the number of particles in the whole slope.

Figure 15 shows that the kinetic energy increases obviously with time at first until $t = 24$ s. Then it decreases gradually with time. The kinetic energy is nearly zero when $t = 60$ s. In comparison with Figs. 10 and 15 show that the kinetic energy of grains and the maximum velocity share a similar pattern, but the former arrives at its peak and zero values earlier than the latter. In addition, the total kinetic energy of grains can be expressed against time by the following empirical equation.

$$E = 0.0964 - 0.000367(t - 24)^2 \tag{4}$$

The prediction by Eq. (4) is also presented in Fig. 15, which demonstrates that Eq. (4) can describe the change of total kinetic energy of grains in the landslide relatively well.

Figure 16 present the kinetic energy of grains of different velocities, which are either larger or smaller than the mean velocity V_m , measured in the DEM landslide analyses. Figure 16 shows that the kinetic energy of grains of velocities larger than V_m is different from that smaller than V_m . There is one peak value in the former but two values in the latter. The kinetic energy of large velocities increases with time at first until $t = 18$ s. Then it decreases gradually with time, approaching nearly zero at $t = 60$ s. In addition, the former accounts for main part of the total kinetic energy between $t = 8$ and $t = 40$, while at other time it is the latter that constitutes the main part of the kinetic energy.

5.2 Velocity range

Figure 17 provides the number of grains of different velocity, which falls into one of the seven groups evenly ranging from

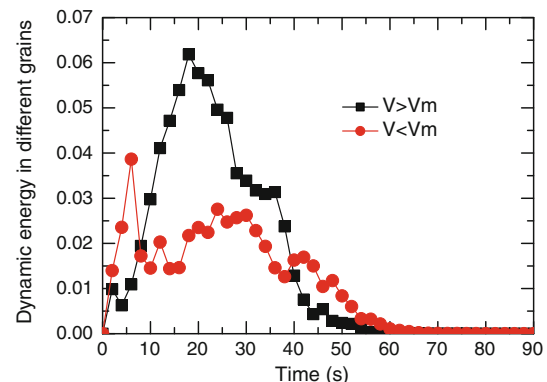


Fig. 16 Kinetic energy of grains of different velocities measured in the DEM landslide analyses, in which V_m represents the mean velocity

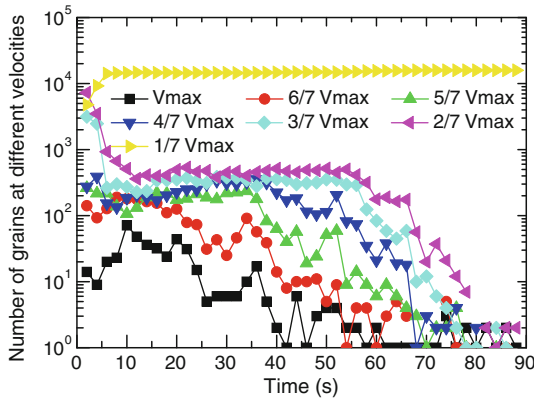


Fig. 17 Number of grains measured at different velocities in the DEM landslide analyses

0 and v_{max} and which is illustrated on the log scale, measured at different time in the DEM landslide analyses. Figure 17 shows that the number of grains at velocity of $(0 - 1/7)v_{max}$ increases obviously with time until $t = 6$ s. Then, it increases slightly with time. In contrast, the number of grains demonstrates a similar pattern against time for those at five ranges of velocity between $1/7v_{max}$ and $6/7v_{max}$, decreasing evidently at first, then slightly, and obviously again with time. However, the number of grains at velocity of $(6/7 - 1)v_{max}$ generally decreases obviously with time, but in a fluctuation way.

5.3 Grain-size effects

Figure 18 presents the number of different-size grains, which diameter d is either larger or smaller than mean diameter d_{50} , at velocity of $(0 - 1/7)v_{max}$ measured in the DEM landslide analyses. Figure 18 shows that the number of grains at velocity of $(0 - 1/7)v_{max}$ increases obviously with time at first until $t = 6$ s, and then increases slightly to its final value, regardless of their sizes. However, the final number for the grains

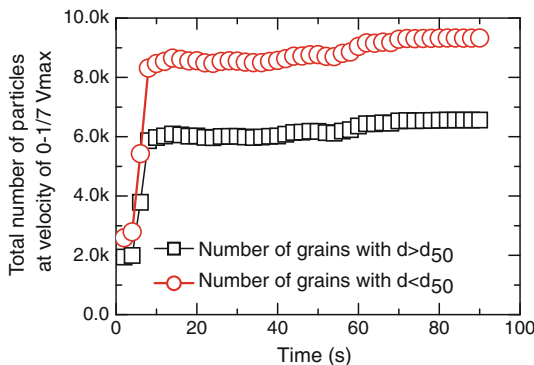


Fig. 18 Number of different-size grains at velocity of $(0 - 1/7)v_{max}$ measured in the DEM landslide analyses

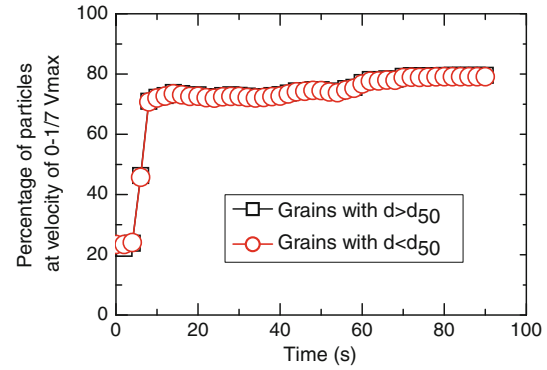


Fig. 19 Percentage of different-size grains at velocity of $(0 - 1/7)v_{max}$ measured in the DEM landslide analyses

of $d > d_{50}$ is larger than that for those of $d < d_{50}$. We shall investigate the reason next.

Figure 19 provides the percentage of different-size grains, either $d > d_{50}$ or $d < d_{50}$ at velocity of $(0 - 1/7)v_{max}$ to the respective total number of grains, measured in the DEM landslide analyses. Figure 19 shows that whether the diameter is larger or smaller than d_{50} , there is a unique relationship between the percentage and time. It increases obviously with time at first until $t = 6$ s, and then increases slightly to its final value, about 80% at $t = 80$ s. It can be deduced from Fig. 19 that it is the difference on the respective total number that leads to the difference on the final number of grains at velocity of $(0 - 1/7)v_{max}$ in Fig. 18. Hence, there is little grain-size effect for the grains at velocity of $(0 - 1/7)v_{max}$.

Table 1 presents the grain-size effect for particles at velocity of $(0 - 1/7)v_{max}$ or $(6/7 - 1)v_{max}$ observed in the DEM analyses. Since the number of the particles at the velocity changes with time or step, the number of particles summed over 45 steps is used to investigate the effect. Hence, the percentage in Table 1 is the averaged percentage of particles to the generated particles. Table 1 shows that there is little grain-size effect for the grains at velocity of $(0 - 1/7)v_{max}$. In contrast, there is an evident grain-size effect for the grains at

Table 1 Grain-size effect for particles at different velocity observed in DEM analyses

Particle velocities	Particle sizes	Number of particles summed over 45 steps	Averaged percentage of particles to the generated (%)	Relative difference (%)
$(0 - 1/7)v_{max}$	$>d_{50}$	269,348	72.22	0.47
	$<d_{50}$	382,561	72.56	
$(6/7 - 1)v_{max}$	$>d_{50}$	225	0.06033	12
	$<d_{50}$	284	0.05387	

The number of generated particles is 11,716 and 8,288 for $d < d_{50}$ and $d > d_{50}$ respectively

velocity of $(6/7 - 1)v_{\max}$. Although there are fewer particles of $d > d_{50}$ than those of $d < d_{50}$ moving at $(6/7 - 1)v_{\max}$, the percentage of $d > d_{50}$ particles is 12 % larger than those of $d < d_{50}$. Hence, it can be deduced from Table 1 that large-size grains tend to move fast during very rapid landslide. This observation is similar to the recent findings on size segregation of spherical pellets in the surface flow, in which the smaller pellets were found to be concentrated near the core of the granular assembly, and the larger pellets segregate to the outer wall [69].

5.4 Post-failure configuration

Post-failure configuration may serve as a basis for remedial measure designs. Figure 20 provides initial and post-failure slopes observed in the DEM analyses. Figure 20 shows that the inclination of the post-failure slope is 13.5° , which is smaller than 45° , the inclination of the initial slope. In addition, this post-failure inclination is much smaller than the peak/residual internal friction angle, i.e., 22.2° and 18.8° respectively shown in Fig. 6. This inclination of the post-failure slope is quite close to the mean value of slope angles (i.e., 14°) in landslide masses investigated in Higashikubiki area, Japan [70]. This observation highlights the difference between the internal friction angle, angles of repose (static and dynamical), and the angle of post-failure slope. Since the angles of repose come from loose material, the static repose angle should be equal or close to the residual internal friction angle, smaller than the peak internal friction angle but significantly larger than the angle of post-failure slope, while the dynamical repose angle should be equal to the angle of post-failure slope. The angle with its tangent defined by the ratio between height and travelled distance is about 37.5° , which is larger than these four angles. Moreover, Fig. 20 shows that the surface of the post-failure slope does not pass through the toe of the initial slope, but through the surface centre of the initial slope. This observation is different from that introduced in any textbook on Soil Mechanics, in which the

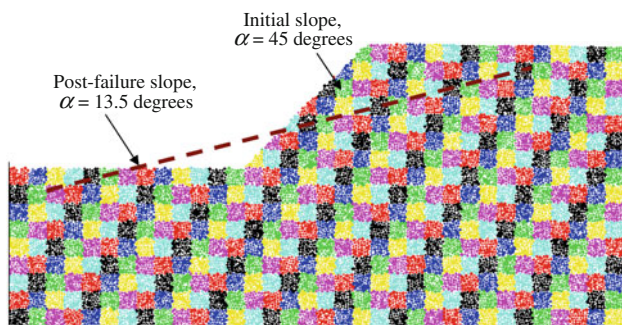


Fig. 20 Initial and post-failure slopes observed in the DEM analyses

failure surface of a granular slope is assumed to be straight line passing through the slope toe in 2-D analyses.

6 Concluding remarks

This study presented a distinct element modeling of one full very-rapid landslide of a bonded granular cut slope which was triggered by an abrupt reduction of bond strength to zero at all inter-particle contacts. This is particularly important for understanding the landslide process, establishing its practical macro-constitutive models, theoretical and numerical analysis methods, and subsequently improving design theories on disaster mitigation. The main feature of the study is that a DEM code *NS2D*, developed by the first author, was used to carry out the numerical test and the results were analyzed from the viewpoint of macroscopic and microscopic geomechanics.

The main conclusions from this study are:

- (1) During the landslide process, the soil moves either in a rather random/chaotic way (diffuse failure) or in different curved shear bands (localized failure). The soil close to slope surface moves along downward slope in a manner that the closer to the slope surface, the larger the displacement, while the soil close to the slope toe moves significantly in the horizontal direction. The closer to the slope surface, the faster the soil moves. In addition, the landslide experiences rapid flow most of the time, with its maximum velocity increasing obviously with time at first to its peak value, then decreasing gradually with time to zero. The kinetic energy of grains and the maximum velocity share a similar pattern, with the former arriving at its peak and final values earlier than the latter.
- (2) During the landslide process, the soil close to slope undergo a repeated loading and unloading process, i.e., fluctuations, and an evident rotation of principal stresses. In addition, their stress state may arrive slightly over or at the peak strength envelope of the material as a result of large deformation rates experienced.
- (3) The number of grains at velocity of $(0 - 1/7)v_{\max}$ increases obviously at first and then slightly with time. In contrast, the number of grains demonstrates a similar pattern against time for those at other five ranges of velocity between $1/7v_{\max}$ and $6/7v_{\max}$, decreasing evidently at first, slightly then, and obviously again with time. However, the number of grains at velocity of $(6/7 - 1)v_{\max}$ generally decreases obviously with time, but in a fluctuation way.
- (4) Regardless of particle sizes, there is a unique relationship between the percentage of different-size grains at

velocity of $(0 - 1/7)v_{\max}$ and time. It increases obviously with time at first, and then increases slightly to its final value. Hence, there is little grain-size effect for the grains at velocity of $(0 - 1/7)v_{\max}$. In contrast, there is an evident grain-size effect for the grains at velocity of $(6/7 - 1)v_{\max}$, with large-size grains tending to move fast during landslide process.

- (5) The post-failure inclination is much smaller than the peak/residual internal friction angle but quite close to the mean value of slope angles in landslide masses investigated in Higashikubiki area, Japan [70]. Moreover, the post-failure slope surface does not pass through the initial slope toe, but through the centre of the initial slope surface.

One of our future works is to employ DEM to investigate the impact of very-rapid granular flow on a barrier [71], its dynamic behavior in mountainous terrain [72], its run-out distances [73], and the effects of the physical parameters on the initiation and/or the propagation of the avalanche, with a reasonable reduction of bond strength at each bond contact and/or with more advanced post-failure contact models [46,74–76].

Acknowledgments The work reported in the paper was funded by China National Funds for Distinguished Young Scientists with grant number 51025932, Major Project of Chinese National Programs for Fundamental Research and Development (973 Program) with grant number 2011CB013504, China National Natural Science Foundation with grant number 51179128, Program for Changjiang Scholars and Innovative Research Team in University with grant number IRT1029, and Japan Society for the Promotion of Science. All these supports are greatly appreciated. In addition, the authors would like to thank the reviewers for their valuable comments on this paper.

References

- Laouafa, F., Darve, F.: Modelling of slope failure by a material instability mechanism. *Comput. Geotech.* **29**, 301–325 (2002)
- Fell, R., Glastonbury, J., Hunter, G.: Rapid landslides: the importance of understanding mechanisms and rupture surface mechanics. The eighth glossop lecture. *Q. J. Eng. Geol. Hydrogeol.* **40**, 9–27 (2007)
- Morgenstern, N.R., Price, V.E.: The analysis of the stability of general slip surfaces. *Geotechnique* **15**(1), 79–93 (1965)
- Sarma, S.K.: Stability analysis of embankments and slopes. *Geotechnique* **23**(3), 423–433 (1973)
- McCombie, P.F.: Displacement based multiple wedge slope stability analysis. *Comput. Geotech.* **36**, 332–341 (2009)
- Sarma, S.K.: Stability analysis of embankments and slopes. *J. Geotech. Eng. (ASCE)* **105**(GT12), 1511–1524 (1979)
- Greve, R., Hutter, K.: Motion of a granular avalanche in a convex and concave curved chute: experiments and theoretical predictions. *Philos. Trans. R. Soc. Lond.* **342**, 573–600 (1993)
- Pouliquen, O., Forterre, Y.: Friction law for dense granular flows: application to the motion of a mass down a rough inclined plane. *J. Fluid Mech.* **453**, 133–151 (2002)
- Ling, H.I., Wu, M.H., Leshchinsky, D., Leshchinsky, B.: Centrifuge modeling of slope instability. *J. Geotech. Geoenviron. Eng. (ASCE)* **135**(6), 758–767 (2009)
- Tohari, A., Nishigaki, M., Komatsu, M.: Laboratory rainfall-induced slope failure with moisture content measurement. *J. Geotech. Geoenviron. Eng. (ASCE)* **133**(5), 575–587 (2007)
- Kulasingam, R., Malvick, E., Boulanger, R.W., Kutter, B.L.: Strength loss and localization at silt interlayers in slopes of liquefied sand. *J. Geotech. Geoenviron. Eng. (ASCE)* **130**(11), 1192–1202 (2004)
- Pastor, M., Blanc, T., Pastor, M.J.: A depth-integrated viscoplastic model for dilatant saturated cohesive-frictional fluidized mixtures: application to fast catastrophic landslides. *J. Non-Newtonian Fluid Mech.* **158**, 142–153 (2009)
- Pastor, M., Haddad, B., Sorbino, G., Cuomo, S., Drempetic, V.: A depth-integrated, coupled SPH model for flow-like landslides and related phenomena. *Int. J. Numer. Anal. Methods Geomech.* **33**, 143–172 (2009)
- Quecedo, M., Pastor, M., Herreros, M.I., Fernandez Merodo, J.A.: Numerical modelling of the propagation of fast landslides using the finite element method. *Int. J. Numer. Methods Eng.* **59**, 755–794 (2004)
- Zornberg, J.G., Mitchell, J.K., Sitar, N.: Testing of reinforced slopes in a geotechnical centrifuge. *Geotech. Test. J. (ASTM)* **20**(4), 470–480 (1997)
- Nova-Roessig, L., Sitar, N.: Centrifuge model study of the seismic response of reinforced soil slopes. *J. Geotech. Geoenviron. Eng. (ASCE)* **132**(3), 388–400 (2006)
- Katz, O., Aharonov, E.: Landslides in vibrating sand box: what controls types of slope failure and frequency magnitude relations? *Earth Planet. Sci. Lett.* **247**, 280–294 (2006)
- Malvick, E.J., Kutter, B.L., Boulanger, R.W.: Post-shaking shear strain localization in a centrifuge model of a saturated sand slope. *J. Geotech. Geoenviron. Eng. (ASCE)* **134**(2), 164–174 (2008)
- Malvick, E.J., Kutter, B.L., Boulanger, R.W., Kulasingam, R.: Shear localization due to liquefaction-induced void redistribution in a layered infinite slope. *J. Geotech. Geoenviron. Eng. (ASCE)* **132**, 1293–1303 (2006)
- Fiegel, G.L., Kutter, B.L.: Liquefaction-induced lateral spreading of mildly sloping ground. *J. Geotech. Eng.* **120**(12), 2236–2243 (1994)
- Whitman, R.V.: On liquefaction. In: *Proceedings of the 11th International Conference on Soil Mechanics and Foundation Engineering*, pp. 1923–1926. San Francisco, Balkema, Rotterdam, The Netherlands (1985)
- Ishihara, K.: Post-earthquake failure of a tailings dam due to liquefaction of the pond deposit. In: *Proceedings of the International Conference on Case Histories in Geotechnical Engineering*, pp. 1129–1143. St. Louis (1984)
- Seed, H.B., Makdisi, F., Idriss, I.M., Lee, K.L.: The slides in the San Fernando Dams during the earthquake of February 9, 1971. *J. Geotech. Eng. Div. (ASCE)* **101**, 651–688 (1975)
- Fernandez Merodo, J.A., Pastor, M., Mira, P., Tonni, L., Herreros, M.I., Gonzalez, E., Tamagnini, R.: Modelling of diffuse failure mechanisms of catastrophic landslides. *Comput. Methods Appl. Mech. Eng.* **193**, 2911–2935 (2004)
- Fell, R.O., Leroueil, S., Riemer, W.: Keynote lecture-geotechnical engineering of the stability of natural slopes, and cuts and fills in soil. In: *Proceeding of the International Conference on Geotechnical and Geological Engineering (Geo Eng 2000)*, pp. 21–120. Melbourne, I. Technomic, Lancaster (2000)
- Hunter, G., Fell, R.: Mechanics of failure of soil slopes leading to 'rapid' failure. In: Picarelli, L. (ed.) *Proceedings, International Conference Fast Slope Movements, Prediction and Prevention for Risk Mitigation*, pp. 283–290. Naples, May 2003. Patron, Bologna (2003)

27. Picarelli, L., Oboni, F., Evans, S., Mostyn, G., Fell, R.: Hazard characterization and quantification. In: Hungr, O., Fell, R., Couture, R., Eberhardt, E. (eds.) *Landslide Risk Management*, pp. 27–62. Balkema, Rotterdam (2005)
28. Gabet, E.J., Mudd, S.M.: The mobilization of debris flows from shallow landslides. *Geomorphology* **74**, 207–218 (2006)
29. Duncan, J.M.: State of the art: limit equilibrium and finite element analysis of slopes. *J. Geotech. Eng. (ASCE)* **122**(7), 577–596 (1996)
30. Borja, R.I.: Free boundary, fluid flow, and seepage forces in excavations. *J. Geotech. Eng. (ASCE)* **118**(1), 125–146 (1992)
31. Griffiths, D.V., Lane, P.A.: Slope stability analysis by finite elements. *Geotechnique* **49**(3), 387–403 (1999)
32. Cundall, P.A., Strack, O.D.L.: The distinct numerical model for granular assemblies. *Géotechnique* **29**(1), 47–65 (1979)
33. Thornton, C.: Numerical simulation of deviatoric shear deformation of granular media. *Géotechnique* **50**(1), 43–53 (2000)
34. Bardet, J.P.: Observations on the effects of particle rotations on the failure of idealized granular materials. *Mech. Mater.* **18**, 159–182 (1994)
35. Jiang, M.J., Zhu, H.H., Li, X.M.: Strain localization analyses of idealized sands in biaxial tests by distinct element method. *Frontiers Archit. Civ. Eng. China (FAC)* **4**(2), 208–222 (2010)
36. Kuhn, M.R., Mitchell, J.K.: New perspectives on soil creep. *J. Geotech. Geoenviron. Eng.* **119**(3), 507–524 (1993)
37. Anandarajah, A.: On influence of fabric anisotropy on the stress-strain behaviour of clays. *Comput. Geotech.* **27**(1), 1–17 (2000)
38. McDowell, G.R., Bolton, M.D.: On the micro mechanics of crushable aggregates. *Geotechnique* **48**(5), 667–679 (1998)
39. Cheng, Y.P., Bolton, M.D., Nakata, Y.: Crushing and plastic deformation of soils simulated using DEM. *Geotechnique* **54**(2), 131–141 (2004)
40. Jiang, M.J., Harris, D., Yu, H.S.: Kinematic models for non-coaxial granular materials: part II: evaluation. *Int. J. Numer. Anal. Methods Geomech.* **29**(7), 663–689 (2005)
41. Jiang, M.J., Harris, D., Zhu, H.H.: Future continuum models for granular materials in penetration analyses. *Granul. Matters* **9**, 97–108 (2007)
42. Jiang, M.J., Leroueil, S., Konrad, J.M.: Insight into shear strength functions of unsaturated granulates by DEM analyses. *Comput. Geotech.* **31**(6), 473–489 (2004)
43. Jiang, M.J., Leroueil, S., Konrad, J.M.: Yielding of micro-structured geomaterial by DEM analysis. *J. Eng. Mech. (ASCE)* **131**(11), 1209–1213 (2005)
44. Jiang, M.J., Yu, H.S., Leroueil, S.: A simple and efficient approach to capturing bonding effect in naturally micro-structured sands by discrete element method. *Int. J. Numer. Methods Eng.* **69**, 1158–1193 (2007)
45. Delenne, J.Y., El Yousoufi, M.S., Cherblanc, F., Beneet, J.C.: Mechanical behaviour and failure of cohesive granular materials. *Int. J. Numer. Anal. Methods Geomech.* **28**, 1577–1594 (2004)
46. Jiang, M.J., Yu, H.S., Harris, D.: Bond rolling resistance and its effect on yielding of bonded granulates by DEM analyses. *Int. J. Numer. Anal. Methods Geomech.* **30**(7), 723–761 (2006)
47. Wang, Y.H., Leung, S.C.: Characterization of cemented sand by experimental and numerical investigations. *J. Geotech. Geoenviron. Eng. (ASCE)* **134**(7), 992–1004 (2008)
48. Jiang, M.J., Yu, H.S., Harris, D.: Discrete element modelling of deep penetration in granular soils. *Int. J. Numer. Anal. Methods Geomech.* **30**(4), 335–361 (2006)
49. Jiang, M.J., Zhu, H.H., Harris, D.: Classical and non-classical kinematic fields of two-dimensional penetration tests on granular ground by discrete element method analyses. *Granul. Matter* **10**, 439–455 (2008)
50. Teufelsbauer, H., Wang, Y., Chiou, M.C., Wu, W.: Flow-obstacle interaction in rapid granular avalanches: DEM simulation and comparison with experiment. *Granul. Matter* **11**, 209–220 (2009)
51. Bharadwaj, R., Wassgren, C., Zenit, R.: The unsteady drag force on a cylinder immersed in a dilute granular flow. *Phys. Fluids* **16**, 1511–1517 (2006)
52. Hanes, D.M., Walton, O.R.: Simulations and physical measurements of glass spheres flowing down a bumpy incline. *Powder Technol.* **109**, 133–144 (2000)
53. Darve, F., Servant, G., Laouafa, F., Khoa, H.D.V.: Failure in geomaterials: continuous and discrete analyses. *Comput. Methods Appl. Mech. Eng.* **193**, 3057–3085 (2004)
54. Utili, S., Nova, R.: DEM analysis of bonded granular geomaterials. *Int. J. Numer. Anal. Meth. Geomech.* **32**, 1997–2031 (2008)
55. Thompson, N., Bennett, M.R., Petford, N.: Analyses on granular mass movement mechanics and deformation, with distinct element numerical modeling: implications for large-scale rock and debris avalanches. *Acta Geotech.* **4**, 233–247 (2009)
56. Okada, Y., Sassa, K., Fukuoka, H.: Excess pore pressure and grain crushing of sands by means of undrained and naturally drained ring-shear tests. *Eng. Geol.* **75**, 325–343 (2004)
57. Jiang, M.J., Konrad, J.M., Leroueil, S.: An efficient technique for generating homogeneous specimens for DEM studies. *Comput. Geotech.* **30**(7), 579–597 (2003)
58. Bolton, M.D., Gui, M.W.: The study of relative density and boundary effects for cone penetration tests in centrifuge. Research report: CUED/D-SOILS/TR256. Dept. of Engrg., Cambridge University, UK (1993)
59. Phillips, R., Valsangkar, A.J.: An experimental investigation of factors affecting penetration resistance in granular soils in centrifuge modelling. Research report: CUED/D-SOILS/TR210. Dept. of Engrg., Cambridge University, UK (1987)
60. Brown, H.E., Holbrook, W.S., Hornbach, M.J., Nealon, J.: Slide structure and role of gas hydrate at the northern boundary of the Storegga Slide, offshore Norway. *Marine Geol.* **229**(3–4), 179–186 (2006)
61. King J.: Tsing shan debris flow. Hong Kong Government. Geotechnical Engineering Office, Special Project Report SPR 1996; 6/96 (1996)
62. Hungr, O.: A model for the runout analysis of rapid flow slides, debris flows and avalanches. *Can. Geotech. J.* **32**, 610–623 (1995)
63. IUGS: A suggested method for describing the rate of movement of landslides. IUGS Work. Group Landslides Int. Assoc. Eng. Geol. Bull. **52**, 75–78 (1995)
64. Jop, P., Forterre, Y., Pouliquen, O.: Initiation of granular surface flows in a narrow channel. *Phys. Fluids* **19**, 88–102 (2007)
65. Josserand, C., Lagree, P.Y., Lhuillier, D.: Stationary shear flows of dense granular materials: a tentative continuum modeling. *Eur. Phys. J. E* **14**, 127–135 (2004)
66. Scott, A.A., Riemer, M.: Collapse of saturated soil due to reduction in confinement. *J. Geotech. Eng. (ASCE)* **121**(2), 216–220 (1995)
67. Iverson, R.M., LaHusen, R.G.: Dynamic pore-pressure fluctuations in rapidly shearing granular materials. *Science* **246**, 796–799 (1989)
68. Nicot, F., Daouadji, A., Laouafa, F., Darve, F.: Second-order work, kinetic energy and diffuse failure in granular materials. *Granul. Matter* **13**, 19–28 (2011)
69. Moysey, P.A., Baird, M.H.I.: Size segregation of spherical nickel pellets in the surface flow of a packed bed: experiments and discrete element method simulations. *Powder Technol.* **196**, 298–308 (2009)
70. Iwahashi, J., Watanabe, S., Furuya, T.: Landform analysis of slope movements using DEM in Higashikubiki area, Japan. *Comput. Geosci.* **27**, 851–865 (2001)

71. Law, R.P.H., Zhou, G.D., Ng, C.W.W., Tang, W.H.: Experimental and three-dimensional numerical investigations of the impact of dry granular flow on a barrier. *Landslides and engineered slopes: from the past to the future*. In: Chen et al. (eds.) *Proceedings of the 10th Int. Symp. on Landslides and Engineered Slope*. 30 June–4 July, 2008, Xi'an, China, Taylor and Francis Group, London, vol. 1, pp. 415–420
72. Lan, H.X., Martin, C.D., Zhou, C.H.: Numerical modeling of debris flow kinematics using discrete element method combined with GIS. *Landslides and engineered slopes: from the past to the future*. In: Chen et al. (eds.) *Proceedings of the 10th Int. Symp. on Landslides and Engineered Slope*. 30 June–4 July, 2008, Xi'an, China, Taylor and Francis Group, London, vol. 1, pp. 769–775
73. Poisel, R., Preh, A.: 3D landslide run out modelling using the particle Flow Code PFC3D. *Landslides and engineered slopes: from the past to the future*. In: Chen et al. (eds.) *Proceedings of the 10th Int. Symp. on Landslides and Engineered Slope*. 30 June–4 July, 2008, Xi'an, China, Taylor and Francis Group, London, vol. 1, pp. 873–879
74. Jiang, M.J., Yu, H.-S., Harris, D.: A novel discrete model for granular material incorporating rolling resistance. *Comput. Geotech.* **32**(5), 340–357 (2005)
75. Jiang, M.J., Leroueil, S., Zhu, H.H., Yu, H.-S., Konrad, J.M.: Two-dimensional discrete element theory for rough particles. *Intern. J. Geomech. (ASCE)* **9**(1), 20–33 (2009)
76. Jiang, M.J., Yan, H.B., Zhu, H.H., Uti, S.: Modeling shear behavior and strain localization in cemented sands by two-dimensional distinct element method analyses. *Comput. Geotech.* **38**(5), 14–29 (2011)